

# Comparison of Planar and 3D Silicon Pixel Sensors Used for Detection of Low Energy Antiprotons

A. Gligorova, *Member, IEEE*, S. Aghion, A. S. Belov, G. Bonomi, P. Bräunig, J. Bremer, R. S. Brusa, L. Cabaret, M. Caccia, R. Caravita, F. Castelli, G. Cerchiari, S. Cialdi, D. Comparat, G. Consolati, J. H. Derking, C. Da Via, S. Di Domizio, L. Di Noto, M. Doser, A. Dudarev, R. Ferragut, A. Fontana, P. Genova, M. Giammarchi, S. N. Gninenko, S. Haider, H. Holmestad, T. Huse, E. Jordan, T. Kaltenbacher, A. Kellerbauer, A. Knecht, D. Krasnický, V. Lagomarsino, S. Lehner, A. Magnani, C. Malbrunot, S. Mariazzi, V. A. Matveev, F. Moia, C. Nellist, G. Nebbia, P. Nédélec, M. Oberthaler, N. Pacifico, V. Petráček, F. Prelz, M. Prevedelli, C. Riccardi, O. Røhne, A. Rotondi, H. Sandaker, M. A. Subieta Vasquez, M. Špaček, G. Testera, E. Widmann, P. Yzombard, S. Zavatarelli, and J. Zmeskal

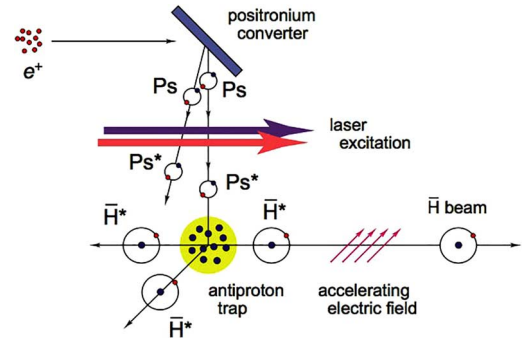


Fig. 1. Principle of the AEgIS antihydrogen beam formation [1].  $\text{Ps}^*$  and  $\text{H}^*$  denote positronium and antihydrogen in Rydberg states respectively.

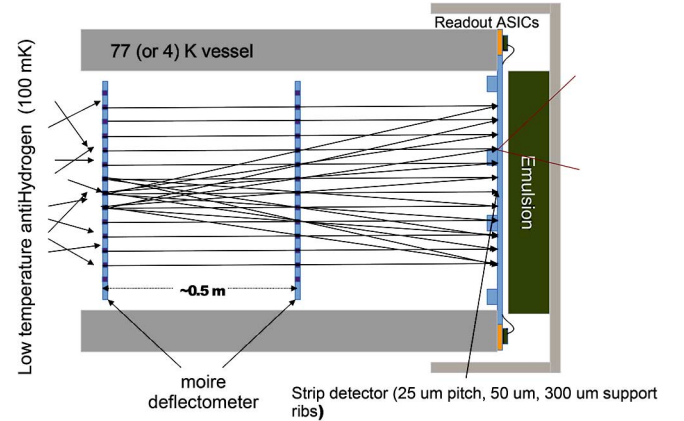


Fig. 2. The gravity module showing the principle of the moiré deflectometer and the position annihilation detectors [14]. Antihydrogen atoms enter from the left side and get reduced in vertical components by the two gratings of the moiré deflectometer. Anti-atoms that reach the silicon detector will annihilate on its surface. The annihilation products are detected by the emulsion detector.

## I. INTRODUCTION

THE main goal of the AEgIS experiment [1] is to measure for the first time directly the Earth's gravitational acceleration of antimatter. To achieve this, AEgIS will produce a beam of antihydrogen, the simplest form of electrically neutral antimatter, and measure its free fall. This measurement would test both the Weak Equivalence Principle, stating that all bodies fall with the same acceleration independently of their mass and

Manuscript received December 13, 2013; revised June 13, 2014; accepted October 16, 2014. Date of publication December 02, 2014; date of current version December 11, 2014.

Please see the Acknowledgment section of this paper for the author affiliations.

composition, as well as General Relativity, which predicts that matter and antimatter should behave identically in the gravitational field of the Earth. Such a result would be important to understand the matter-antimatter asymmetry as observed in the Universe. Moreover, certain theories consider the existence of a mutual repulsive force between matter and anti-matter (called antigravity) which could eliminate the need for dark matter [2], [3].

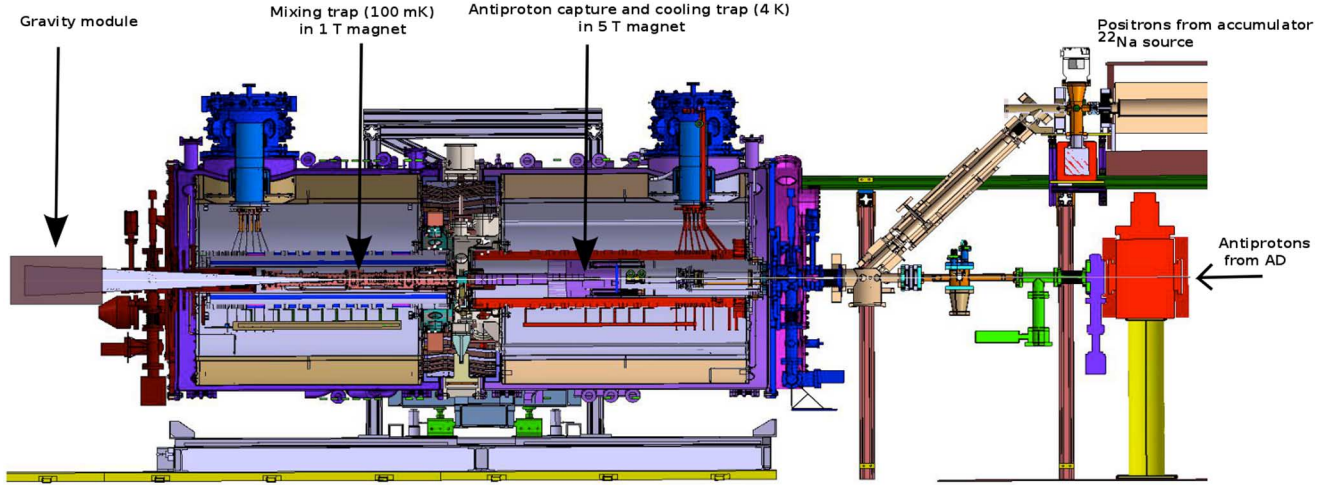


Fig. 3. Schematic view of the AEgIS apparatus. It consists of two magnets, 5 T and 1 T, which enclose the antiproton trap and the mixing trap respectively. The antiproton decelerator (AD) provides 5.3 MeV antiprotons which are trapped and cooled down in the 5 T magnet. The positrons are guided towards the main apparatus by their own transfer line. After the positronium is produced, it is mixed with the antiprotons in the 1 T magnet to form the antihydrogen atoms. The produced antihydrogen is formed into a beam through Stark acceleration. The gravity module is attached at the end of the 1 T magnet.

In order to obtain the first experimental result on this subject, the AEgIS experiment is currently being constructed at the antiproton decelerator (AD) [4] at CERN. During its first phase of operation the goal is to measure the gravitational interaction of antihydrogen with 1% precision.

#### A. Principle of Antihydrogen Formation and Detection

Antihydrogen atoms in AEgIS will be formed by a resonant charge exchange reaction between Rydberg ( $n \sim 20$ -30) positronium and cold (100 mK) antiprotons (see Fig. 1). The antihydrogen states will thus be defined by the positronium states. The positrons will be supplied from a  $^{22}\text{Na}$  source and will be guided towards a slab of nanoporous silica which acts as a positronium converter [5]. The antiprotons (5.3 MeV), supplied by the AD, will be first trapped and cooled down in the catching traps inside the 5 T magnet (Fig. 3), before being sent to the mixing trap in the 1 T magnet where the resonant charge exchange reaction takes place. After this, an inhomogeneous electric field, i.e., Stark acceleration [6] is applied to form the antihydrogen atoms into a pulsed beam. In flight, some of the antihydrogen paths will be selected by passing through the two gratings of a moiré deflectometer [7], which operates in the classical regime (see Fig. 2). After about 1 m of free fall, the selected antihydrogen atoms will be detected with a position sensitive detector, consisting of a thin (50  $\mu\text{m}$ ) silicon strip detector followed by an emulsion detector [8] and a scintillating fiber telescope. The vertical shift of the fringe pattern formed by the moiré deflectometer is proportional to the value of  $g$  experienced by antihydrogen. If the distance between the gratings and the detector is 0.5 m, the vertical shift is expected to be  $\sim 20 \mu\text{m}$ . For this reason, a position resolution better than  $\sim 10 \mu\text{m}$  is needed [9].

#### B. Antiproton Annihilation

To study the detector response it is important to understand the annihilation process of antihydrogen in silicon. As the positron annihilates immediately with the electron cloud, antihydrogen annihilations can be studied using antiprotons.

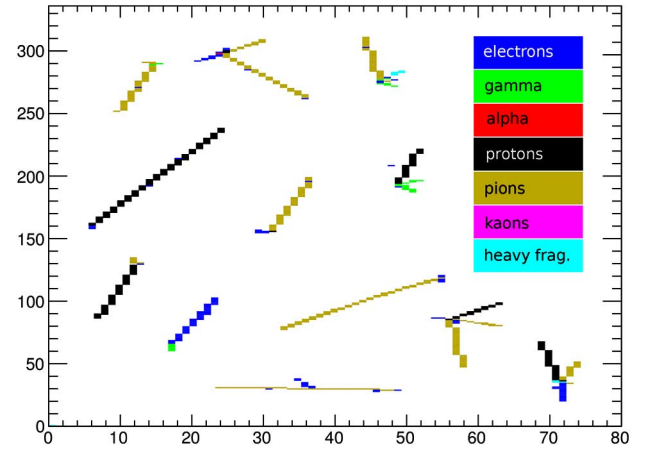


Fig. 4. Samples of simulated annihilation events (GEANT4, Fritjof-Precompound model) in a silicon pixel sensor (pixel size:  $250 \times 50 \mu\text{m}$ , thickness 230  $\mu\text{m}$ ). Fill code applied to the pixels identifies the particle with the major contribution to the energy deposition in the single pixel cell. The multiplicity of different annihilation prongs predicted by this model is given in [14, Fig. 5].

The annihilation of an antiproton with a nucleus produces on average four charged pions. If the nucleus has a high  $Z$ -number, the pions may interact with other nucleons and cause the nuclei to fragment with the emission of ions. Among other particles that can be produced in this process are alpha particles, photons, electrons, and heavy ions [10].

Detection of annihilation prongs and thus the identification of the annihilation signature can be made by using silicon detectors since they are sensitive to charged particles like protons and charged pions. Fig. 4 shows typical signatures from simulated annihilation events in a 3D silicon pixel sensor. The tracks of the annihilation products make possible to reconstruct the position where the antiproton annihilation took place.

Pions and energetic protons, due to their relatively low energy deposition, can travel long distances in silicon (up to few cm). Heavy ions are characterized by a localized deposition of a large fraction of their energy. Detection of long tracks allows

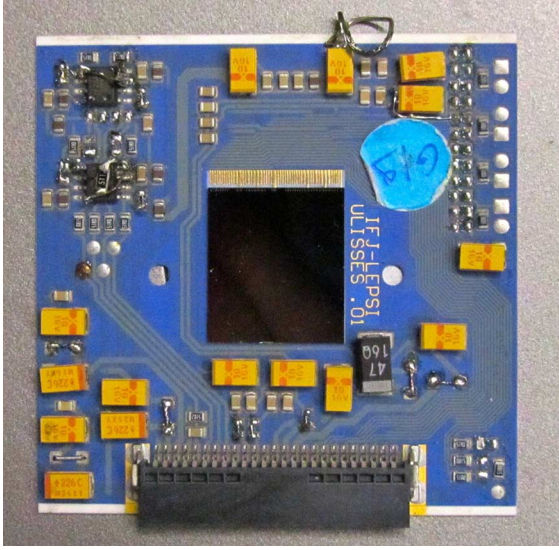


Fig. 5. The MAPS detector mounted on its PCB. The dimensions of the sensor are  $\sim 2 \times 2 \text{ cm}^2$ .

reconstruction of the annihilation point by extrapolation, while detection of the energy deposited locally by heavy fragments can provide direct information on the annihilation position.

In the present work we report on the comparison of two different detector technologies, thin monolithic active pixel (MAPS) and 3D pixel sensor. It will be shown that both technologies have position reconstruction capabilities. While MAPS is more sensitive to highly ionizing particles, 3D performs better for low/minimum ionizing particles.

## II. TEST BEAM WITH ANTIPROTONS

The main motivation for this study was to test the concept of using silicon sensors as position sensitive annihilation detectors. This is the first step towards the development and construction of a silicon annihilation detector with a resolution better than  $10 \text{ }\mu\text{m}$ .

Detection of on-sensor annihilations of antiprotons in silicon has been performed only once to our knowledge, in an experiment using antiprotons with a momentum of  $608 \text{ MeV}/c$  and a non-segmented sensor [11]. Direct annihilations of antiprotons on an emulsion surface have also been investigated for the AEgIS experiment [8]. In other experiments silicon micro-strip detectors were used for detection of the end products of antihydrogen annihilations that happened somewhere else [12], [13]. The vertex associated with the annihilation point was then reconstructed from the prong tracks.

In our case, during the two beam test periods we detected on-sensor annihilations of antiprotons in segmented silicon sensors. The AD supplied the initial antiproton beam with a momentum of  $100 \text{ MeV}/c$  (kinetic energy of  $5.3 \text{ MeV}$ ). The particles were further slowed down with several degraders, reaching the energy value of few  $100 \text{ keV}$  according to simulations [14], just before impinging on the detector.

### A. First Measurements with Monolithic Active Pixel Sensor

The first detector that we tested was a monolithic active pixel sensor (MAPS), called MIMOTERA [15]. The MAPS was installed in vacuum ( $\sim 10^{-6} \text{ mbar}$ , at room temperature) in a six

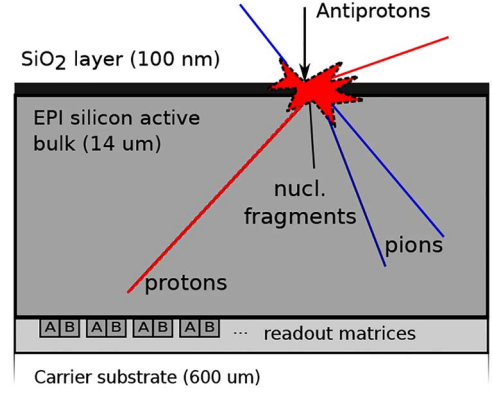


Fig. 6. Schematic view (not to scale) of the MAPS detector, showing an annihilation event occurring in the first layers of the detector and annihilation prongs travelling inside the sensitive volume.

way cross which was attached at the end of the main AEgIS apparatus. Here it could detect a fraction of the antiprotons not caught by the traps in the  $5 \text{ T}$  magnet. A photo of this detector mounted on a PCB is shown in Fig. 5. Its total size is  $\sim 2 \times 2 \text{ cm}^2$ , the epitaxial layer is  $14 \text{ }\mu\text{m}$  thick and the pixel pitch is  $153 \text{ }\mu\text{m}$ . The original wafer is glued on a silicon mechanical support of  $\sim 600 \text{ }\mu\text{m}$  thick amorphous silicon and thinned down from the backside, until only a very thin passivation layer covers the sensitive volume. The MAPS is back-illuminated through this entrance window with a thickness of  $\sim 100 \text{ nm}$  ( $\text{SiO}_2$ ). The maximum readout rate is configurable up to  $20 \text{ MHz}$ . The readout system of the detector is divided into four sub-arrays of  $28 \times 112$  pixels, which are read out in parallel. Every pixel consists of two independent readout matrices, each of them built by  $2 \times 81$  interconnected diodes,  $5 \times 5 \text{ }\mu\text{m}^2$  respectively. This double-readout architecture allows the MAPS to operate without dead-time. The detector was mounted  $\sim 4 \text{ cm}$  off axis (the same position was used for the 3D sensor, described later on) in order to have a lower luminosity. In this way only the antiprotons deviated by the  $5 \text{ T}$  fringe field were detected, permitting the study of individual clusters.

The simulated kinetic energy distribution of the antiprotons implies that most of them annihilate within the first few microns of this detector [14]. Fig. 6 shows the cross-section of the MAPS as well as an illustration of an antiproton annihilation including the tracks of typical products.

### B. Second Measurements with 3D Pixel Sensor

The small thickness and the relatively low granularity of the MAPS detector, as well as the high dynamic range provided important information on the typical energy range of the clusters and, accordingly, the required dynamic range of the final detector.

To be able to study the tracks from the annihilation prongs in more detail and to estimate the achievable resolution of the annihilation point, we chose to test a pixel detector with larger thickness. Such a sensor allowed observing tracks generated from annihilations at shallow angles, crossing the detector sideways.

The 3D pixel sensor (CNM 55) [16], manufactured by CNM, was installed during the second beam test in AEgIS (Fig. 7). The position of the detector inside the six way cross was the same



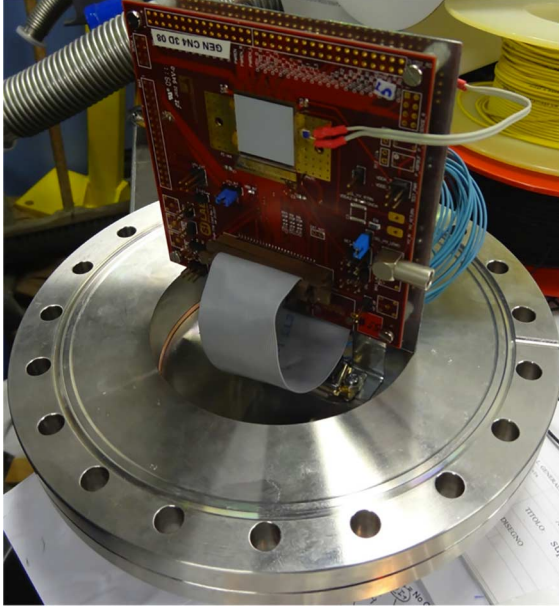


Fig. 7. The 3D sensor bump bonded to the FE-I4 readout chip, mounted on a single chip card. The whole system is mounted on a flange before being installed in vacuum in the six way cross.

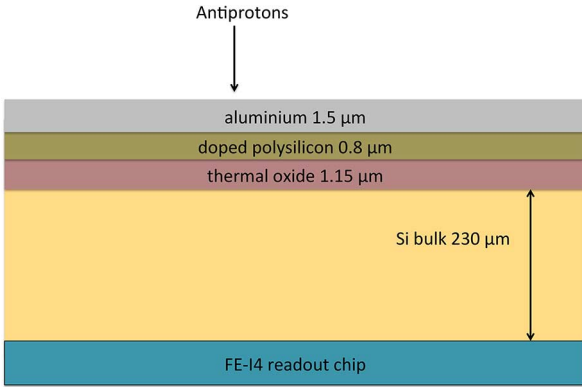


Fig. 8. Schematic view (not to scale) of the cross section of the 3D detector with the different layers on top.

as for the MAPS detector, providing as similar conditions with the first beam test as possible.

This 3D pixel sensor and the readout ASIC [17] were originally designed for the *Insertable B Layer* [18] currently being installed at the ATLAS [19] experiment at CERN, optimized for looking at high energy particles from events occurring every 25 ns. In addition to permitting studies of the beam profile, this technology offered interesting features relevant for our application as described below.

The sensor consists of 80 (columns)  $\times$  336 (rows) = 26 880 cells. The pixel size is  $250 \times 50 \mu\text{m}^2$  and the electrodes have a diameter of  $10 \mu\text{m}$ . The thickness of the active volume is  $230 \mu\text{m}$  and its passivation layer is composed of  $1.15 \mu\text{m}$  thermal oxide and  $0.8 \mu\text{m}$  doped poly-silicon, one on top of the other. A  $1.5 \mu\text{m}$  thick layer of aluminium is deposited at the end. A schematic view of the cross-section of the detector is given in Fig. 8, while an overview of the architecture of one pixel is given in Fig. 9. The internal box drawn with a dotted line represents a typical cell that consists of two readout

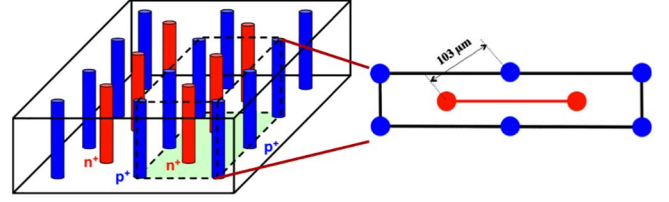


Fig. 9. Schematic view of the 3D electrodes in the 3D pixel sensor. The volume within the dashed lines represents one pixel consisting of two readout ( $n^+$ , inner) and six ohmic ( $p^+$ , outer) electrodes.

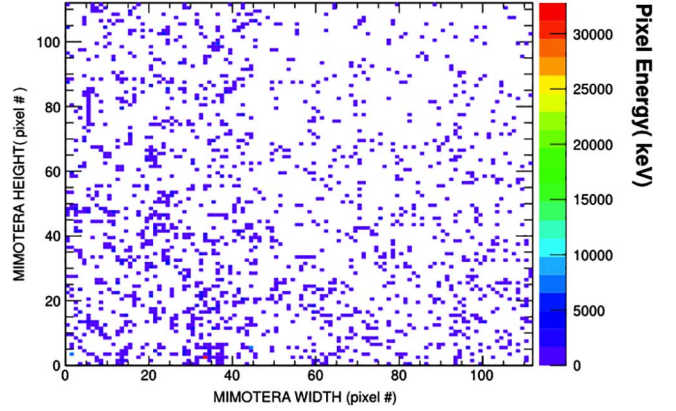


Fig. 10. Sample of a triggered frame from the monolithic planar pixel detector after applying the noise cut, showing clusters up to 30 MeV.

n-columns around six ohmic p-columns. The 3D design of the electrodes results in several advantages over the planar pixel technology, like a lower depletion voltage and a shorter collection path, allowing a shorter charge collection time [20]. The readout was performed with the USBpix custom DAQ system, USBpix hardware [21], [22], based on a multipurpose IO-board (S3MultiIO) with a USB2.0 interface to a PC and an adapter card which connects the S3MultiIO to the single chip adapter card (SCC). The FE-I4 and the sensor are mounted on the SCC. The S3MultiIO system contains a programmable (Xilinx XC3S1000 FG320 4C) FPGA, which provides and handles all signals going to the front end chip.

### III. RESULTS

#### A. Monolithic Planar Sensor

The results of the MAPS detector are fully reported in [14]. What follows is a summary of the features of antiproton annihilations in a planar pixel detector to be compared with the second measurement using the 3D detector. In these first tests we successfully detected on-sensor annihilations for the very first time at such low antiproton energies. Some areas of the detector were covered with 3, 6, and  $9 \mu\text{m}$  Al foil for studying the number of annihilations in each of them. These areas are excluded from the following analyses. The analogue readout of the MAPS detector required an off-line noise cut. This cut was fixed to 150 keV, the value being extracted as 5 RMS (30.3 keV) from the noise distribution of single pixels. A sample frame (after the noise cut) is shown in Fig. 10.

For the cluster analysis, clusters were defined as conglomerates of pixels neighboring in the horizontal, vertical, and diagonal direction, without using a seed-driven algorithm. This

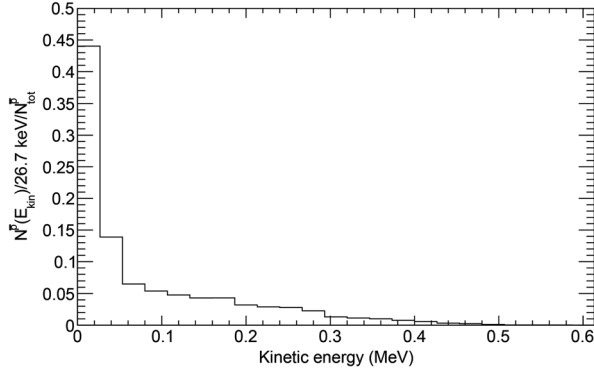


Fig. 11. Kinetic energy distribution for the incoming antiprotons impinging on the 3D sensor.

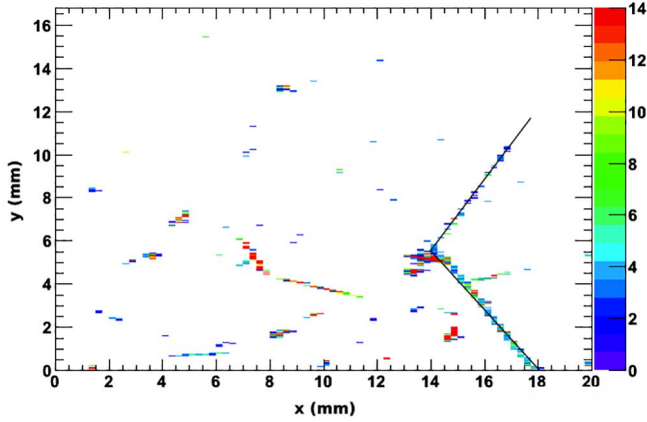


Fig. 12. Sample hitmap of the 3D sensor with two fitted proton tracks coming from an antiproton annihilation. Such long tracks are used to reconstruct the annihilation point.

would require assumptions on the geometrical profile of the energy deposited, which is not possible due to the heterogeneous nature of the clusters. In spite of the small detector thickness, the relatively high statistics allowed the observation of 21 clusters that contained tracks. These tracks originated from long-range annihilation products travelling inside the thin detector plane. We found prongs (most likely being protons) with lengths up to 2.9 mm.

The position resolution for the MAPS depends on the topology of the event. For annihilations where a single pixel is fired, the resolution is equivalent to the pixel cell ( $153 \mu\text{m}$ ). This is also the case for clusters with a well defined center (seed). Degradation of the resolution occurs in widespread clusters with relatively uniform energy, in other words, when no seed (usually a heavy ion releasing several MeV in one pixel) can be determined.

### B. 3D Sensor

The tests with the 3D sensor allowed for more detailed studies of the antiproton annihilation in silicon, in particular of tracks of the annihilation prongs. Since both the MAPS and 3D detector were placed at the same position, the energy distributions for the incoming antiprotons were similar. This distribution is given in Fig. 11. A sample acquisition frame is shown in Fig. 12. When compared to the typical frame of the thin monolithic detector, more and longer tracks can be observed, as a result of the thicker active volume. As the prongs are equally distributed

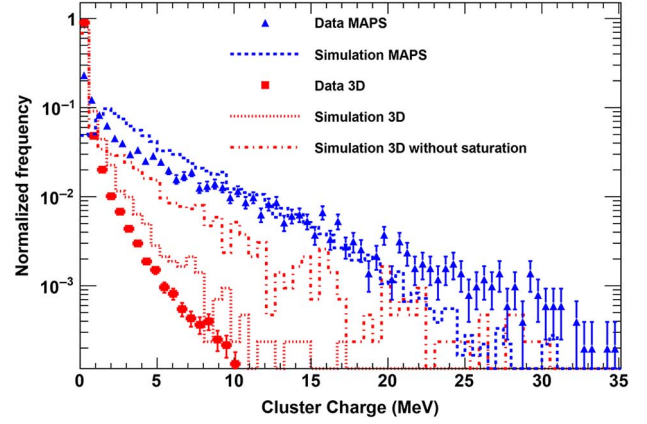


Fig. 13. Cluster energy distribution for the MAPS and 3D pixel sensors. Also shown are the respective simulation results in GEANT4. All distributions are normalized to unit integral.

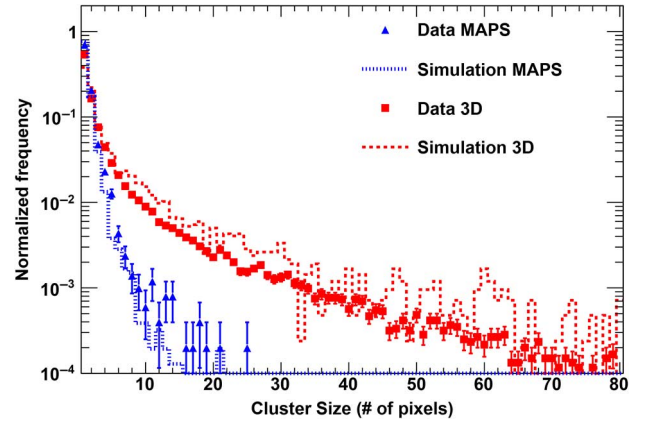


Fig. 14. Cluster size distribution for the MAPS and 3D pixel sensors. Also shown are the respective simulation results in GEANT4. All distributions are normalized to unit integral.

in  $4\pi$ , tracks are more likely due to the higher geometrical acceptance for annihilation products travelling at angles different from the direction of the beam.

When travelling through the detector, the particles produce tracks from a few mm to 1.5 cm long. As a proof of principle, the positions of ten annihilation points were reconstructed by linear fitting of the non-weighted track points and propagating the errors of the parameters of the straight line to the interception point (Fig. 12). The position resolution that was achieved calculating the errors on the coordinates of the interception point is  $56.5 \mu\text{m}$  on X (pixel size of  $250 \mu\text{m}$ ) and  $24.3 \mu\text{m}$  on Y (pixel size of  $50 \mu\text{m}$ ). An improvement of the resolution could be achieved with a sensor not affected by pixel saturation, by using weighted fitting algorithms, taking into account the charge of the pixels in the tracks.

### C. Detector Comparison and Simulations

Two cluster parameters, the total cluster energy and the cluster size are compared for the two sensor types and with Monte Carlo simulations. Plots for the cluster energy are shown in Fig. 13 while plots for cluster size are shown in Fig. 14.

For the MAPS sensor, the small ratio depth/pixel width resulted in small clusters of mostly one pixel ( $\sim 70\%$ ), about 20%

of two pixels, and the remaining part included clusters composed of three or more pixels. The cluster energy was measured to be up to 40 MeV [14]. Charge saturation of pixels from the generation of slow charged fragments characterized by a high  $dE/dx$  was observed in very few ( $< 10$ ) annihilation events. This is due to the high dynamic range of the detector.

In [14], the one pixel clusters of the MAPS detector was found to be, in part, due to secondary particles from annihilations happening elsewhere in the apparatus. This background effect was simulated separately and also studied in the data. However, for the 3D sensor, the simulation of the background did not show a definite topology (clusters of different sizes are produced by background due to the thicker bulk). Hence, to allow a better comparison, the values and plots reported in the present work include all clusters for both the 3D and MAPS detector. The background contamination of the total number of events is estimated to 16% and needs to be taken into account when interpreting the results for both sensors.

For the 3D sensor we observe large clusters due to having many long tracks, even as large as 80 pixels. Cluster energy is lower than what was observed with the MAPS detector. One of the main reasons for this discrepancy is to be found in two parameters: the thicker passivation region which is more likely to stop heavy fragments that would produce high energy deposits and a higher frequency of low energy events to which the MAPS detector is not sensitive. In addition to this, saturation of the single channel amplifiers was often observed (35% of all hit pixels were saturated in the 3D detector): the measured charge is thus expected to be lower than the charge effectively deposited in the bulk in some cases.

The mean cluster size for the 3D sensor is found to be  $3.93 \pm 0.031$  pixels, for the MAPS  $1.54 \pm 0.005$ . As for the cluster energy, the mean value for the 3D sensor is  $0.29 \pm 0.003$  MeV, while for the MAPS it is  $4.47 \pm 0.023$  MeV.

The cluster parameters (size and energy) from data analysis were compared with GEANT4 [23], [24] simulations. The simulation was performed using the Fritjof-Precompound physics list which has shown to provide the best description of annihilation events among the models embedded in GEANT4. A more detailed description of simulations including references to the AEgIS simulation framework can be found in [14].

For both cluster energy and cluster size, GEANT4 simulations provided a partial description of the experimental data, reproducing well the differences between the two different kind of sensors.

For the MAPS detector, the cluster energy distribution in Fig. 13 shows an excess of clusters with energy  $< 1$  MeV in the data compared with simulations.

A smaller excess in cluster energy is observed in simulations for the 3D sensor, though in this case the range in cluster energy is limited, in both data and simulations, by the saturation of the single pixel channels. Fig. 13 also includes the energy deposited in the 3D sensor with no saturation accounted for. The higher sensitivity of the 3D sensor to long travelling particles is well reflected also in simulations for the 3D sensor by a cluster sizes in excess of 80 pixels.

#### IV. CONCLUSION

In this work we have presented results obtained using segmented silicon for the detection of direct on-sensor antiproton

annihilations. The purpose of the work has been to determine if standard silicon sensor technology can be used to directly detect annihilation of antihydrogen and, in particular, if such technology is suitable for the AEgIS silicon annihilation detector. As direct detection of annihilation in silicon has not been extensively studied before, two types of pixel detectors (monolithic planar pixel and 3D pixel) were selected to also be able to study the precise topology of an annihilation event in a silicon sensor. Regardless of the differences, both sensors were able to correctly detect annihilation events. The analysis of the obtained data showed the impact of the detector characteristics on the response to an antimatter annihilation event. The results will allow fine tuning of the AEgIS sensor design to the best trade-off between position resolution and detector efficiency.

The MAPS detector, with its high saturation limit, allowed measurement of the localized energy released in an annihilation event, with a mean value measured in the order of several MeV. The 3D sensor was instead able to prove the principle of using a segmented sensor to detect tracks of lower ionizing products, which could ideally be adopted in the construction of a tracking detector, i.e., a silicon telescope.

The most important findings of this work can be summarized as follows:

- Total energy deposition up to 10 MeV per antiproton annihilation for the 3D detector (up to 40 MeV for the MAPS).
- Identification of tracks from annihilation prongs up to 1.5 cm long in the 3D detector (2.9 mm in the case of MAPS).
- Comparison and partial agreement with GEANT4 Fritjof-Precompound model for the size and the charge of the clusters produced from the antiproton annihilation. The simulation proved to account for the intrinsic technological differences in the two sensors.
- Position resolution of  $56.5 \mu\text{m}$  for X and  $24.3 \mu\text{m}$  for the Y coordinate of the annihilation point in the 3D sensor. A better resolution could be achieved by employing weighted fitting with a saturation-free readout.

As the final silicon detector to be installed in AEgIS has a thickness requirement of  $\leq 50 \mu\text{m}$  in order to be transparent for pions and protons to be detected in the downstream detectors, it is relying on the detection of highly ionising annihilation products for the position reconstruction. Enhanced resolution is expected due to the small thickness (reducing sensitivity to sidewise travelling products) and by using a strip detector with a finer pitch of  $25 \mu\text{m}$ . A detailed study, focussing on the design to achieve a resolution better than  $10 \mu\text{m}$  is currently being carried out. For improved position resolution (down to  $1 \mu\text{m}$ ) and for measurement redundancy, the silicon annihilation detector will be used in combination with other tracking detectors, together composing the AEgIS gravity module.

#### ACKNOWLEDGMENT

The authors would like to thank the Bergen Research Foundation and the Research Council of Norway for their support to this project. The authors also thank Ole Dorholt for the technical support and the ATLAS 3D community for putting their detector at the authors' disposal and their help with the testing. The research leading to these results has received funding from the European Research Council under the European Union's Seventh Framework Programme (FP7/2007-2013)/ERC Grant

agreement no [291242] and the Austrian Ministry for Science and Research. Finally the authors thank Andrea Micelli for his support throughout the test-beam campaign with the 3D CNM-55 sensor.

A. Gligorova, N. Pacifico, and H. Sandaker are with the Institute of Physics and Technology, University of Bergen, 5007 Bergen, Norway (e-mail: angela.gligorova@cern.ch).

S. Aghion and F. Moia are with Politecnico di Milano, 20133 Milano, Italy, and Istituto Nazionale di Fisica Nucleare, 20133 Milano, Italy.

A. S. Belov and S. N. Gninenko are with the Institute for Nuclear Research of the Russian Academy of Sciences, Moscow 117312, Russia.

G. Bonomi and M. A. Subieta Vasquez are with the Department of Mechanical and Industrial Engineering, University of Brescia, 25133 Brescia, Italy, and Istituto Nazionale di Fisica Nucleare, 27100 Pavia, Italy.

P. Bräunig and M. Oberthaler are with the Kirchhoff Institute for Physics, University of Heidelberg, 69120 Heidelberg, Germany.

J. Bremer, J. H. Derking, M. Doser, A. Dudarev, S. Haider, T. Kaltenbacher, and A. Knecht are with the Physics Department, European Organisation for Nuclear Research, 1211 Geneva 23, Switzerland.

R. S. Brusa and L. Di Noto are with the Department of Physics and TIFPA-INFN, University of Trento, 38123 Povo, Trento, Italy.

L. Cabaret, D. Comparat, and P. Yzombard are with Laboratoire Aimé Cotton, CNRS, Université Paris Sud, ENS Cachan, Bâtiment 505, Campus d'Orsay, 91405 Orsay Cedex, France.

M. Caccia is with Insubria University, Como-Varese, Italy.

R. Caravita, F. Castelli, and S. Cialdi are with the Department of Physics and Istituto Nazionale di Fisica Nucleare, University of Milano, 20133 Milano, Italy.

G. Cerchiari, E. Jordan, and A. Kellerbauer are with Max Planck Institute for Nuclear Physics, 69117 Heidelberg, Germany.

G. Consolati and R. Ferragut are with Politecnico di Milano, Piazza Leonardo da Vinci 32, 20133 Milano, Italy, and Istituto Nazionale di Fisica Nucleare, Sez. di Milano, Via Celoria 16, 20133 Milano, Italy.

C. Da Via and C. Nellist are with the University of Manchester, Oxford Road, Manchester M13 9PL, U.K.

S. Di Domizio, D. Krasnický, G. Testera, and S. Zavatarelli are with Istituto Nazionale di Fisica Nucleare, Sez. di Genova, Via Dodecaneso 33, 16146 Genova, Italy.

A. Fontana and P. Genova are with Istituto Nazionale di Fisica Nucleare, Sez. di Pavia, Via Agostino Bassi 6, 27100 Pavia, Italy.

M. Giammarchi and F. Prelz are with Istituto Nazionale di Fisica Nucleare, Sez. di Milano, Via Celoria 16, 20133 Milano, Italy.

H. Holmestad, T. Huse, and O. Röhne are with the University of Oslo, Department of Physics, Sem Sælands vei 24, 0371 Oslo, Norway.

V. Lagomarsino is with the University of Genoa, Department of Physics, Via Dodecaneso 33, 16146 Genova, Italy.

S. Lehner, S. Mariazzi, E. Widmann, and J. Zmeskal are with Stefan Meyer Institut für subatomische Physik, Boltzmannsgasse 3, 1090 Vienna, Austria.

A. Magnani, C. Riccardi, and A. Rotondi are with the University of Pavia, Department of Nuclear and Theoretical Physics, Via Bassi 6, 27100 Pavia, Italy, and Istituto Nazionale di Fisica Nucleare, Sez. di Pavia, Via Agostino Bassi 6, 27100 Pavia, Italy.

C. Malbrunot is with European Organisation for Nuclear Research, Physics Dept., 1211 Geneva 23, Switzerland, and Stefan Meyer Institut für subatomische Physik, Boltzmannsgasse 3, 1090 Vienna, Austria.

V. A. Matveev is with the Institute for Nuclear Research of the Russian Academy of Sciences, Moscow 117312, Russia, and Joint Institute for Nuclear Research, 141980 Dubna, Russia.

G. Nebbia is with Istituto Nazionale di Fisica Nucleare, Sez. di Padova, Via Marzolo 8, 35131 Padova, Italy.

P. Nédélec is with Claude Bernard University Lyon 1, Institut de Physique Nucléaire de Lyon, 4 Rue Enrico Fermi, 69622 Villeurbanne, France.

V. Petráček and M. Špaček are with Czech Technical University in Prague, FNSPE, Břehová 7, 11519 Praha 1, Czech Republic.

M. Prevedelli is with the University of Bologna, Department of Physics, Via Irnerio 46, 40126 Bologna, Italy.

## REFERENCES

- [1] A. Kellerbauer, M. Amoretti, and A. S. Belov *et al.*, “Proposed antimatter gravity measurement with an antihydrogen beam,” *Nucl. Instrum. Methods Phys. Res. B*, vol. 266, pp. 351–356, 2008.

- [2] M. Villata, “CPT symmetry and antimatter gravity in general relativity,” (*EPL*) *Europhys. Lett.*, vol. 94, p. 20001, 2011.
- [3] M. Villata, “Dark energy,” *Local Void Astrophys. Space Sci.*, vol. 339, no. 7, 2012.
- [4] S. Maury, “The antiproton decelerator,” *Hyperfine Interactions*, vol. 109, no. 1–4, pp. 43–52, 1997.
- [5] G. Consolati, R. Ferragut, A. Galarneau, F. Di Renzo, and F. Quasso, “Mesoporous materials for antihydrogen production,” *Chem. Soc. Rev.*, vol. 42, pp. 3821–3832, 2013.
- [6] G. Testera, A. S. Belov, and G. Bonomi *et al.*, “Formation of a cold antihydrogen beam in AEGIS for gravity measurements,” in *AIP Conf. Proc.*, 2008, vol. 1037, no. 5.
- [7] M. K. Oberthaler, S. Bernert, E. M. Rasel, J. Schmiedmayer, and A. Zeilinger, “Inertial sensing with classical atomic beams,” *Phys. Rev. A*, vol. 54, pp. 3165–3176, 1996.
- [8] M. Kimura, S. Aghion, and O. Ahlén *et al.*, “Development of nuclear emulsions with 1 m spatial resolution for the AEGIS experiment,” *Nucl. Instrum. Methods Phys. Res. A*, vol. 732, pp. 325–329, 2013.
- [9] “The AEGIS collaboration proposal for the AEGIS experiment at the CERN antiproton decelerator,” SPSC-P-334. CERN-SPSC-2007-017, 2007 [Online]. Available: <http://cds.cern.ch/record/1037532/files/spsc-2007-017.pdf>
- [10] G. Bendiscioli and D. Kharzeev, “Antinucleon-nucleon and antinucleon-nucleus interaction: A review of experimental data,” *Rivista del Nuovo Cimento, Series 3*, vol. 17, no. 6, pp. 1–142, Jun. 1994.
- [11] P. L. McGaughey, N. J. DiGiacomo, W. E. Sonndheim, J. W. Sunier, and Y. Yariv, “Low energy antiproton-nucleus annihilation radius selection using an active silicon detector/target,” *Nucl. Instrum. Methods*, vol. 249, pp. 361–365, 1986.
- [12] C. Regenfus, “A cryogenic silicon micro-strip and pure-CsI detector for detection of antihydrogen annihilations,” *Nucl. Instrum. Methods Phys. Res. A*, vol. 501, pp. 6571–.
- [13] G. B. Andersen, M. D. Ashkezari, and W. Bertsche *et al.*, “Antihydrogen annihilation reconstruction with the ALPHA silicon detector,” *Nucl. Instrum. Methods Phys. Res. A*, vol. 684, pp. 73–81, 2012.
- [14] S. Aghion, O. Ahlén, and A. S. Belov *et al.*, “Detection of low energy antiproton annihilations in a segmented silicon detector,” *J. Instrum.*, vol. 9, 2014, P06020.
- [15] R. Boll, M. Caccia, C. P. Welsch, and M. H. Holzschneider, “Using monolithic active pixel sensors for fast monitoring of therapeutic hadron beams,” *Radiat. Meas.*, vol. 46, no. 12, pp. 1971–1973, 2011.
- [16] S. Grinstein, M. Baselga, and M. Boscardin *et al.*, “Beam test studies of 3d pixel sensors irradiated non-uniformly for the ATLAS Forward Physics Detector,” *Nucl. Instrum. Methods Phys. Res. A*, vol. 730, pp. 28–32, 2013.
- [17] V. Zivkovic *et al.*, “The FE-I4 pixel readout system-on-chip resubmission for the insertable B-Layer project,” *J. Instrum.*, vol. 7, 2012, C02050.
- [18] C. Da Via *et al.*, “3D silicon sensors: Design, large area production and quality assurance for the ATLAS IBL pixel detector upgrade,” *Nucl. Instrum. Methods Phys. Res. A*, vol. 694, pp. 321–330, 2012.
- [19] The ATLAS Collaboration, *The Performance of the ATLAS Detector*. New York, Springer, The ATLAS Collaboration, , 2011, Reprinted from *Eur. Phys. J. C*, Vols. 70 and 71, 2010 and 2011, CERN for the benefit of the ATLAS collaboration.
- [20] L. Rossi, P. Fischer, T. Rohe, and N. Wermes, *Pixel Detectors: From Fundamentals to Applications*. New York: Springer, 2006.
- [21] M. Backhaus, M. Barbero, and L. Gonella *et al.*, “Development of a versatile and modular test system for ATLAS hybrid pixel detectors,” *Nucl. Instrum. Methods Phys. Res. A*, vol. 650, p. 3740, 2011.
- [22] “The USBpix test system homepage,” [Online]. Available: <http://icwiki.physik.uni-bonn.de/wiki/bin/view/Systems/UsbPix>
- [23] S. Agostinelli, J. Allison, and K. Amako *et al.*, “Geant4—A simulation toolkit,” *Nucl. Instrum. Methods Phys. Res. A*, vol. 506, pp. 250–303, 2003.
- [24] J. Allison, K. Amako, and J. Apostolakis *et al.*, “Geant4 developments and applications,” *IEEE Trans. Nucl. Sci.*, vol. 53, no. 1, pp. 270–278, Feb. 2006.